
DISENTANGLING ALEATORIC AND EPISTEMIC UNCERTAINTY IN PHYSICS-INFORMED NEURAL NETWORKS. APPLICATION TO INSULATION MATERIAL DEGRADATION PROGNOSTICS

A PREPRINT

Ibai Ramirez^{1*} Jokin Alcibar^{1*} Joel Pino² Mikel Sanz^{3,5} Jose I. Aizpurua^{4†}

¹Department of Electronics & Computing, Mondragon University

²CARTIF Technology Centre

³Department of Physical Chemistry, University of the Basque Country (EHU)

⁴Department of Computer Science and Artificial Intelligence, University of the Basque Country (EHU)

⁵Basque Centre for Applied Mathematics (BCAM)

January 8, 2026

Keywords Physics informed Neural Networks, Bayesian Neural Networks, Uncertainty Quantification, Prognostics & Health Management, Insulation

ABSTRACT

Physics-Informed Neural Networks (PINNs) provide a framework for integrating physical laws with data. However, their application to Prognostics and Health Management (PHM) remains constrained by the limited uncertainty quantification (UQ) capabilities. Most existing PINN-based prognostics approaches are deterministic or account only for epistemic uncertainty, limiting their suitability for risk-aware decision-making. This work introduces a heteroscedastic Bayesian Physics-Informed Neural Network (B-PINN) framework that jointly models epistemic and aleatoric uncertainty, yielding full predictive posteriors for spatiotemporal insulation material ageing estimation. The approach integrates Bayesian Neural Networks (BNNs) with physics-based residual enforcement and prior distributions, enabling probabilistic inference within a physics-informed learning architecture. The framework is evaluated on transformer insulation ageing application, validated with a finite-element thermal model and field measurements from a solar power plant, and benchmarked against deterministic PINNs, dropout-based PINNs (d-PINNs), and alternative B-PINN variants. Results show that the proposed B-PINN provides improved predictive accuracy and better-calibrated uncertainty estimates than competing approaches. A systematic sensitivity study further analyzes the impact of boundary-condition, initial-condition, and residual sampling strategies on accuracy, calibration, and generalization. Overall, the findings highlight the potential of Bayesian physics-informed learning to support uncertainty-aware prognostics and informed decision-making in transformer asset management.

1 Introduction

Prognostics and health management (PHM) is a health management paradigm that encompasses predictive methodologies aimed at improving the reliability and availability of engineering components and systems [1]. PHM lies at the core of condition monitoring technologies, where engineering and physical principles, and monitored data are jointly used to develop anomaly detection, diagnostics, prognostics, and maintenance planning applications. The main objective of failure prognostics models is the reliable prediction of the future degradation trajectory of an asset and the estimation of its remaining useful life (RUL) [2].

*Equal Contribution

†Corresponding author: joxe.aizpurua@ehu.eus

Scientific Machine Learning (SciML) has emerged as a transformative paradigm for solving scientific and engineering problems by embedding physical structure directly into machine learning models [3]. Representative developments in SciML include Physics-Informed Neural Networks (PINNs) [4], Neural Operators [5], Physics-Informed Neural Operators (PINO) [6], Kolmogorov–Arnold Networks (KANs) [7], and related approaches designed to learn solutions of governing equations or physical dynamics from data [8]. By incorporating partial differential equations (PDEs) and mechanistic constraints during training, these models typically achieve improved sample efficiency and enhanced generalization compared with purely data-driven methods.

Within the broader PHM literature, hybrid prognostics approaches have historically combined physics-of-failure models with machine learning methods for RUL estimation, relying on sound engineering and physical principles [9, 10, 11]. Such hybrid approaches generally follow either a sequential architecture, in which physics-based model outputs inform a machine learning model [12, 13], or a parallel architecture, where physics-based and machine learning predictions are fused [14, 15]. Hybrid prognostics approaches share conceptual similarities with SciML, but they usually lack a unified learning framework in which physics and data jointly shape the solution.

In prognostics, the RUL is defined as the temporal distance between the prediction time instant, denoted by t_p , and the end of the useful life of the asset, referred to as the end-of-life (EOL). This quantity is commonly estimated by forecasting the future ageing evolution of the system and identifying the expected failure threshold crossing time. The ageing evolution from t_p to EOL is inherently stochastic and affected by multiple sources of uncertainty, including sensor noise, operational variability, and model uncertainty. Consequently, uncertainty quantification (UQ) is essential for reliable RUL predictions.

The application of PINNs to prognostics has recently been explored in domains such as battery degradation modelling [16] and transformer ageing based on heat diffusion physics [17]. However, to the best of the authors’ knowledge, the majority of existing PINN-based prognostics models remain fully deterministic, despite the critical importance of uncertainty quantification for informed decision-making [18, 19]. This limitation is particularly restrictive in realistic PHM scenarios, where data are often sparse, noisy, and heterogeneous, and where multiple sources of uncertainty, such as model misspecification, parameter variability, and measurement noise, must be explicitly accounted for.

Within the SciML community, several uncertainty-aware PINN formulations have been proposed. Bayesian PINNs (B-PINNs) replace deterministic Neural Networks (NNs) with Bayesian Neural Networks (BNNs), enabling the estimation of epistemic uncertainty [20]. Alternative approaches include Gaussian process–augmented PINNs [21], Hamiltonian Monte Carlo–based epistemic PINNs (EPINNs) [22], conformalized PINNs (C-PINNs) providing distribution-free uncertainty guarantees [23], as well as more computationally tractable methods such as dropout-PINNs (d-PINNs) [24] and deep ensemble PINNs [25, 26]. Despite these methodological advances, most studies are restricted to synthetic PDE benchmarks, and their applicability to real-world prognostics problems remains largely unexplored.

More importantly, existing uncertainty-aware PINN approaches rarely provide a comprehensive treatment of total predictive uncertainty by explicitly disentangling epistemic and aleatoric components [27]. Epistemic uncertainty reflects uncertainty in the model structure and parameters due to limited data, whereas aleatoric uncertainty arises from measurement noise and inherent system variability. In PHM applications, the separation and propagation of both uncertainty sources are critical for robust risk assessment and maintenance decision-making [18, 19].

Table 1 summarizes representative SciML and hybrid PHM approaches, highlighting whether they model aleatoric and/or epistemic uncertainty, explicitly disentangle uncertainty sources, adhere to SciML principles, and address PHM applications.

Table 1: Comparison of SciML and hybrid PHM methods, including relevant features for this work.

Method	Aleatoric	Epistemic	Disentanglement	SciML	PHM	Method
[28]	✗	✓	✗	✗	Material	BNN
[29]	✓	✓	✓	✗	Battery	RNN
[16]	✗	✗	✗	✓	Battery	PINN
[17]	✗	✗	✗	✓	Transformer	PINN
[20]	✗	✓	✗	✓		B-PINN
[23]	✓	✗	✗	✓		C-PINN
[22]	✗	✓	✗	✓		EPINN
[24]	✓	✓	✗	✓		d-PINN
[26]	✓	✓	✗	✓		EnsPINN
This Work	✓	✓	✓	✓	Transformer	B-PINN

In this context, it can be observed that PINN-based prognostics models have predominantly relied on deterministic formulations. While uncertainty-aware PINNs have been proposed within the SciML community, to the best of the authors' knowledge, they (i) do not explicitly disentangle aleatoric and epistemic sources of uncertainty, and (ii) have largely been evaluated on controlled synthetic benchmarks rather than realistic PHM applications.

Motivated by the need for uncertainty-aware SciML methods for reliable prognostics, the main contribution of this work is the development of a total UQ framework for PINNs that jointly captures aleatoric and epistemic uncertainty in prognostics applications. The proposed methodology is based on B-PINNs, which integrate PDE-based ageing physics with Bayesian inference over Neural Network (NN) parameters. Extending previous work that mainly focused on epistemic UQ [30], a novel B-PINN architecture is introduced that enables explicit modelling and separation of epistemic and aleatoric sources of uncertainty.

This work demonstrates that incorporating epistemic and heteroscedastic aleatoric uncertainty within B-PINNs yields more reliable and interpretable probabilistic predictions than B-PINNs that model epistemic and homoscedastic uncertainty, as well as deterministic and dropout-based PINN alternatives. The proposed methodology improves predictive accuracy, enhances uncertainty calibration, and increases robustness under noisy and sparse data, which are essential properties for enabling trustworthy prognostics predictions in critical power assets.

This research further contributes with a systematic analysis of the influence of initial-condition, boundary-condition, and residual sampling strategies on generalization and uncertainty calibration, offering new insights into training stability and robustness. The proposed approach is validated with a real-world transformer insulation ageing case study, supported by finite element modelling and operational data from a floating solar power plant. The validated results are supported by a comprehensive benchmarking, which compares B-PINNs with d-PINNs in two different total UQ configurations: (i) epistemic and heteroscedastic aleatoric UQ and (ii) epistemic and homoscedastic aleatoric UQ, along with vanilla deterministic PINNs baselines.

The remainder of this article is organized as follows. Section 2 presents the proposed methodology. Section 3 describes the experimental setup, results, and sensitivity analyses. Section 4 concludes the paper. Appendix A details the transformer thermal and ageing models and Appendix B defines the probabilistic evaluation metrics and benchmarking models.

2 Methods

Figure 1 shows the proposed methodology for the total UQ of Bayesian-PINN models, including epistemic and (heteroscedastic) aleatoric sources of uncertainty.

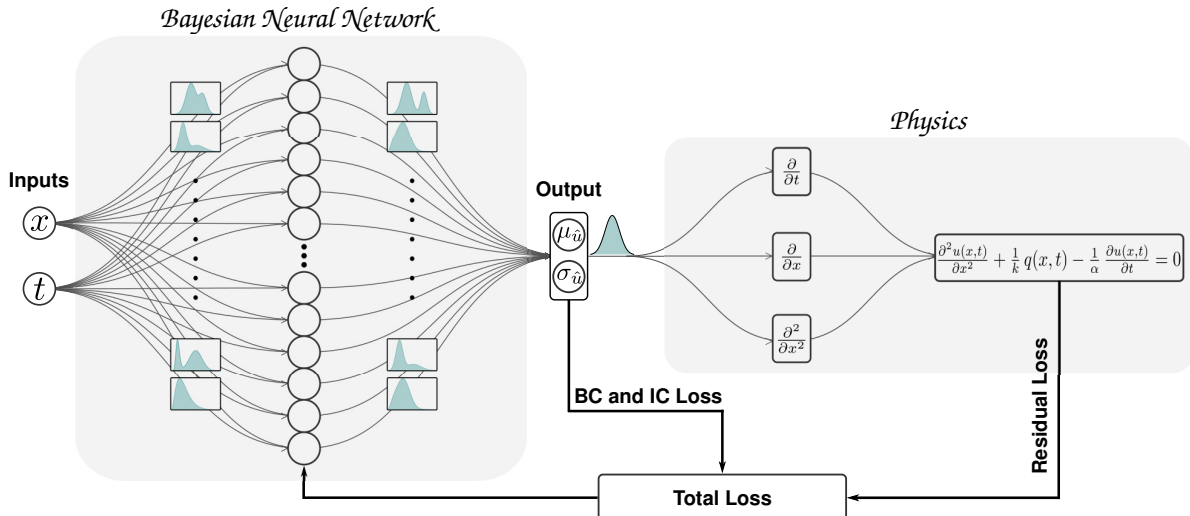


Figure 1: Proposed B-PINN approach for the probabilistic spatiotemporal transformer thermal model, including spatiotemporal inputs, (x, t) , a BNN with probability distribution function over its parameters, two output variables over the solution (u) of the PDE under study ($\mu_{\hat{u}}, \sigma_{\hat{u}}^2$), the physics residual loss, and initial and boundary condition losses integrated in the total loss, which is used to update BNN parameter distributions.

BNNs are used to integrate Bayesian inference into PINNs, enabling principled uncertainty quantification. BNNs capture the epistemic uncertainty of the B-PINN model by modelling the uncertainty associated with the NN parameters. For the quantification of aleatoric uncertainty, a modification of the classical B-PINN model architecture presented in [30] is proposed. Assuming that the uncertainty can be captured with an equivalent Gaussian distribution, the proposed B-PINN model outputs two variables, the mean value of the solution \hat{u} and the variance of the solution $\sigma_{\hat{u}}^2$. The adoption of these two outputs requires modifying the loss function so that the B-PINN learning process is directed by the underlying PDE, regularized by Bayesian principles, and integrates aleatoric and epistemic uncertainties (detailed in Subsection 2.3).

The proposed approach is tested on the electrical transformer insulation material ageing estimation. The insulation ageing estimation approach is based on a spatiotemporal thermal stress model, which drives the insulation ageing model, modeled with an empirical ageing estimation approach.

The thermal stress estimation is done in two steps: (i) the insulation oil temperature estimation, $\hat{\Theta}_o(x, t)$, which is calculated using a 1D heat diffusion PDE with Dirichlet boundary conditions, implemented using the proposed B-PINN approach. (ii) The oil temperature is used to calculate the spatiotemporal winding temperature, $\hat{\Theta}_w(x, t)$, through an empirical winding temperature estimation model. Finally, the insulation ageing estimate, $\hat{V}(x, t)$, is obtained by using the winding temperature, which defines the ageing rate and it is directly used to estimate the insulation RUL [31]. Modelling epistemic and aleatoric sources of uncertainty enables the quantification of the probabilistic estimates of oil temperature, $p(\hat{\Theta}_o(x, t))$, winding temperature, $p(\hat{\Theta}_w(x, t))$, and ageing estimates, $p(\hat{V}(x, t))$. Figure 2 shows the insulation ageing estimation process.

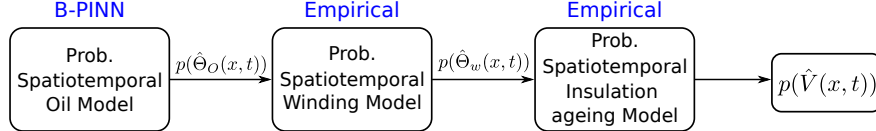


Figure 2: Overall framework for probabilistic transformer insulation ageing estimation. The Bayesian PINN-based model estimates the spatiotemporal oil temperature of the insulation, $\hat{\Theta}_o(x, t)$, which is coupled with an empirical model, which calculates the transformer winding temperature, $\hat{\Theta}_w(x, t)$, and finally, the estimated thermal stress is used to calculate the insulation ageing model $p(\hat{V}(x, t))$, through an empirical approach.

The main focus of this section is on the B-PINN method for total uncertainty quantification. Detailed insulation thermal modelling process, along with insulation ageing estimation modelling equations are provided in Appendix A. Accordingly, Subsection 2.1 introduces PINN basics, Subsection 2.2 defines BNNs, Subsection 2.3 describes the B-PINN approach, and finally Subsection 2.4 defines the total uncertainty quantification process.

2.1 PINN basics

PINNs were introduced with the goal of encoding physics models based on PDEs in machine learning (ML) models [32], taking advantage of the ability of NNs to act as universal approximators [33]. A general PDE can be written as [34]:

$$d\{u(x, t)\} = f(x, t) \quad (1)$$

where $x, t \in \mathbb{R}$ denote position and time, $u(x, t)$ is the unknown solution, d is the differential operator, and $f(x, t)$ is a forcing function introducing external influences.

PINNs consist of the NN part, in which the inputs define temporal ($t \in \mathbb{R}$) and spatial coordinates ($x \in \mathbb{R}$ for one-dimensional cases) for the initial conditions (IC) and boundary conditions (BC). The NN output is an approximated PDE solution at the space and time coordinates, denoted $\hat{u}(x, t)$. This is calculated through the iterative application of weights (w), biases (b), and non-linear activation functions (σ) over the input. Namely, the inputs are connected through neurons, where they are multiplied with the weights and summed with the bias term. Finally, the weighted sum is passed through an activation function (σ). Subsequently, the outcome $\hat{u}(x, t)$ is post-processed via automatic differentiation to compute the derivatives in space and time at certain collocation points (CP), generated via random sampling in the interior of the domain. The PINN is trained at these CPs by minimizing the residuals of the underlying PDE.

The loss function, $\mathcal{L}(\theta, \lambda_0, \lambda_b, \lambda_r)$, incorporates the prediction error of the NN at IC and BC, and the residual of the PDE estimated via automatic differentiation at CP:

$$\mathcal{L}(\boldsymbol{\theta}, \lambda_0, \lambda_b, \lambda_r) = \mathcal{L}_0(\boldsymbol{\theta}, \lambda_0) + \mathcal{L}_b(\boldsymbol{\theta}, \lambda_b) + \mathcal{L}_r(\boldsymbol{\theta}, \lambda_r) \quad (2)$$

where $\boldsymbol{\theta} = \{\mathbf{w}, \mathbf{b}\}$ are the weights and bias terms of the NN, and $\mathcal{L}_0(\boldsymbol{\theta}, \lambda_0)$, $\mathcal{L}_b(\boldsymbol{\theta}, \lambda_b)$, and $\mathcal{L}_r(\boldsymbol{\theta}, \lambda_r)$ are, respectively, the loss terms corresponding to IC, BC, and the residual of the PDE with their corresponding weights, λ_0 , λ_b , and λ_r , defined as follows:

$$\mathcal{L}_0(\boldsymbol{\theta}, \lambda_0) = \lambda_0 \frac{1}{N_0} \sum_{i=1}^{N_0} |\hat{u}(x_i, 0) - u(x_i, 0)|^2 \quad (3)$$

$$\mathcal{L}_b(\boldsymbol{\theta}, \lambda_b) = \lambda_b \frac{1}{N_b} \sum_{i=1}^{N_b} |\hat{u}(x_i, t_i) - u(x_i, t_i)|^2 \quad (4)$$

$$\mathcal{L}_r(\boldsymbol{\theta}, \lambda_r) = \lambda_r \frac{1}{N_r} \sum_{i=1}^{N_r} |r(x_i, t_i)|^2 \quad (5)$$

where N_0 , N_b , and N_r are, respectively, the number of IC, BC, and residual points, while $u(x_i, t_i)$ and $r(x_i, t_i)$ denote the known solution and the residual of PDE, for each training point i defined at the coordinates (x_i, t_i) . According to the PDE defined in Eq. (1), the residual $r(x, t)$ is defined as follows:

$$r(x, t) = d\{u(x, t)\} - f(x, t) \quad (6)$$

Unlike classical NNs, which only minimize the prediction error at measurement points, PINNs enforce governing physics throughout the domain.

Minimizing the loss function in Eq. (2) using a suitable optimization algorithm provides an optimal set of NN parameters $\boldsymbol{\theta} = \{\mathbf{w}, \mathbf{b}\}$. That is, approximating the PDE becomes equivalent to finding $\boldsymbol{\theta}$ values that minimize the loss with a predefined accuracy. Overall, the key training parameters include: number of neurons and number of layers, number of CP, activation function, and the optimizer. Finding the correct solution requires knowing IC and BC. Additionally, random locations (x_i, t_i) , named CP, are used to evaluate the residual loss in Eq. (5).

The main motivation for using PINNs over numerical methods is the computational effort and adaptability to different solutions. Numerical models require a mesh of parameters to model and evaluate the PDE. As for PINNs, there is no need to define the whole mesh.

2.2 Bayesian Neural Networks

BNNs aim to estimate the posterior parameter distribution $P(\boldsymbol{\theta}|\mathcal{D})$, from a training dataset $\mathcal{D} = \{\mathbf{x}^{(i)}, \mathbf{y}^{(i)}\}$, of a set of NN parameters $\boldsymbol{\theta}$:

$$P(\boldsymbol{\theta}|\mathcal{D}) = \frac{P(\mathcal{D}|\boldsymbol{\theta})P(\boldsymbol{\theta})}{P(\mathcal{D})} \quad (7)$$

where $P(\mathcal{D}|\boldsymbol{\theta})$ is the likelihood, $P(\boldsymbol{\theta})$ is the prior, *i.e.* prior knowledge of NN parameters expressed as a PDF over $\boldsymbol{\theta}$, and $P(\mathcal{D})$ is the marginal likelihood.

The likelihood is often estimated from the individual product of pointwise estimated likelihoods $p_i(\mathcal{D}|\boldsymbol{\theta})$ based on the normal distribution $N(\mu, \sigma)$ defined as follows:

$$P(\mathcal{D}|\boldsymbol{\theta}) = \prod_{i=0}^N p(y^{(i)}|x^{(i)}, \boldsymbol{\theta}) \quad (8)$$

$$p(y^{(i)} | x^{(i)}, \boldsymbol{\theta}) = \frac{1}{\sqrt{2\pi}\sigma} \exp\left(-\frac{\|y^{(i)} - \hat{u}(x^{(i)}, \boldsymbol{\theta})\|^2}{2\sigma^2}\right) \quad (9)$$

The selection of a good prior distribution, $P(\boldsymbol{\theta})$, for BNNs is challenging [35]. The most common choice is to use a non-informative prior, which follows a Gaussian distribution with mean zero and unit variance, $\mathcal{N}(0, 1)$, *i.e.* isotropic

Gaussian prior. In addition to the isotropic Gaussian prior, there are alternative non-informative priors that can be used for an improved posterior prediction in terms of accuracy and uncertainty. Without loss of generality, based on previous experience testing different priors [30], this research implements the Laplace prior, defined as follows:

$$P(\boldsymbol{\theta})_{\text{Laplace}} = \prod_{i=1}^d \frac{\lambda}{2} \exp(-\lambda|\theta_i|) \quad (10)$$

where $\lambda > 0$ is the scale parameter, and d is the dimensionality of $\boldsymbol{\theta}$. The Laplace prior also promotes sparsity due to its sharp peak at zero and heavier tails compared to the non-informative Gaussian prior [35].

The analytical posterior in BNNs, $p(\boldsymbol{\theta}|\mathcal{D})$, is intractable, and therefore approximation methods are required. In this work, Variational Inference (VI) is used to approximate the true posterior with a variational distribution $q(\boldsymbol{\theta}|\boldsymbol{\phi})$ of known functional form by minimizing the Kullback–Leibler (KL) divergence between them. Since the true posterior cannot be computed explicitly, this optimization is performed indirectly by maximizing the Evidence Lower Bound (ELBO). In practice, as learning is formulated as a minimization problem, ELBO maximization is equivalently implemented by minimizing its negative, commonly referred to the variational free energy. The resulting optimization objective is defined as follows:

$$\mathcal{L}(\mathcal{D}, \boldsymbol{\phi}) = \text{KL}[q(\boldsymbol{\theta} | \boldsymbol{\phi}) \parallel p(\boldsymbol{\theta})] - \mathbb{E}_{q(\boldsymbol{\theta}|\boldsymbol{\phi})}[\log p(\mathcal{D} | \boldsymbol{\theta})] \quad (11)$$

The first term is the KL divergence between the variational distribution $q(\boldsymbol{\theta}|\boldsymbol{\phi})$ and the prior $p(\boldsymbol{\theta})$ (known as the complexity cost). The second term is the expected value of the likelihood with respect to the variational distribution (known as the likelihood cost). The cost function can be also written as:

$$\mathcal{L}(\mathcal{D}, \boldsymbol{\phi}) = \mathbb{E}_{q(\boldsymbol{\theta}|\boldsymbol{\phi})}[\log q(\boldsymbol{\theta}|\boldsymbol{\phi})] - \mathbb{E}_{q(\boldsymbol{\theta}|\boldsymbol{\phi})}[\log p(\boldsymbol{\theta})] - \mathbb{E}_{q(\boldsymbol{\theta}|\boldsymbol{\phi})}[\log p(\mathcal{D}|\boldsymbol{\theta})] \quad (12)$$

It can be observed from Eq. (12) that loss terms are expectations with respect to the variational distribution $q(\boldsymbol{\theta}|\boldsymbol{\phi})$. Therefore, the cost function can be approximated by Monte Carlo (MC) sampling, drawing K samples $\boldsymbol{\theta}^{(k)}$ from $q(\boldsymbol{\theta}|\boldsymbol{\phi})$:

$$\mathcal{L}(\mathcal{D}, \boldsymbol{\phi}) \approx \frac{1}{K} \sum_{k=1}^K [\log q(\boldsymbol{\theta}^{(k)}|\boldsymbol{\phi}) - \log p(\boldsymbol{\theta}^{(k)}) - \log p(\mathcal{D}|\boldsymbol{\theta}^{(k)})] \quad (13)$$

Throughout this paper, the variational posterior is assumed to follow a Gaussian distribution $\boldsymbol{\phi} = (\boldsymbol{\mu}, \boldsymbol{\sigma})$, where $\boldsymbol{\mu}$ is the mean vector of the distribution and $\boldsymbol{\sigma}$ is the standard deviation vector.

2.3 Bayesian Physics Informed Neural Networks

Bayesian PINNs extend standard PINNs by replacing the deterministic NN with a Bayesian NN. This enables the estimation of epistemic uncertainty, which reflects the model's lack of complete knowledge [36]. In practice, epistemic uncertainty is quantified by placing probability density functions (PDFs) over the BNN parameters.

The main outcome of interest in the B-PINN approach is the posterior distribution. This is calculated following the Bayes rule [cf. Eq. (7)]. Namely, the prior distribution is assumed to be given based on *a priori* knowledge. The likelihood, $P(\mathcal{D}|\boldsymbol{\theta})$, is estimated for the initial point, boundary condition points, and residual samples assuming a Gaussian distribution [cf. Eq. (9)], defined as follows:

$$\begin{aligned} p(u_0|x_0, \boldsymbol{\theta}^{(k)}) &= \prod_{i=1}^{N_0} \frac{1}{\sqrt{2\pi}\sigma_0} \exp\left(-\frac{\|u_0 - \hat{u}(x_0^{(i)}, 0; \boldsymbol{\theta}^{(k)})\|^2}{2\sigma_0^2}\right) \\ p(u_{bc}|x_{bc}, t_{bc}, \boldsymbol{\theta}^{(k)}) &= \prod_{i=1}^{N_{bc}} \frac{1}{\sqrt{2\pi}\sigma_{bc}} \exp\left(-\frac{\|u_{bc} - \hat{u}(x_{bc}^{(i)}, t_{bc}^{(i)}; \boldsymbol{\theta}^{(k)})\|^2}{2\sigma_{bc}^2}\right) \\ p(r(x_f, t_f; \boldsymbol{\theta}^{(k)})) &= \prod_{i=1}^{N_f} \frac{1}{\sqrt{2\pi}\sigma_f} \exp\left(-\frac{\|r(x_f^{(i)}, t_f^{(i)}; \boldsymbol{\theta}^{(k)})\|^2}{2\sigma_f^2}\right) \end{aligned} \quad (14)$$

where σ_0 , σ_{bc} , and σ_f denote the standard deviation of initial, boundary, and residual points.

For computational tractability and efficiency, the log-likelihood terms are considered by taking the logarithm of Eq. (14). Subsequently, the ELBO loss defined for a generic BNN [cf. Eq. (13)], is adapted for B-PINN posterior inference:

$$\mathcal{L}^{(k)} = \log q(\boldsymbol{\theta}^{(k)} | \mathbf{w}) - \log p(\boldsymbol{\theta}^{(k)}) - \lambda_0 \log p(u_0 | x_0, \boldsymbol{\theta}^{(k)}) - \lambda_b \log p(u_{bc} | x_{bc}, t_{bc}, \boldsymbol{\theta}^{(k)}) - \lambda_r \log p(r | x_f, t_f, \boldsymbol{\theta}^{(k)}) \quad (15)$$

This process results in the approximation of the variational posterior distribution $q(\boldsymbol{\theta} | \mathbf{w})$. The training process of the B-PINN approach is shown in Appendix B.2, Algorithm 2.

It is worth highlighting that the variance terms in Eq. (14), if kept constant, they model constant aleatoric uncertainty, known as homoscedastic uncertainty, *i.e.* constant variance. The limitation of homoscedastic uncertainty is that the uncertainty is fixed by the user and held constant throughout the analysis. If this assumption can be relaxed (as proposed in this work), automatically learning aleatoric uncertainty from data presents a data-adaptive uncertainty modelling strategy, *i.e.* heteroscedastic uncertainty.

2.4 Uncertainty Quantification

The modified B-PINN model provides predictive distributions by (i) placing a posterior over the network parameters, which induces epistemic uncertainty, and (ii) producing an input-dependent predictive variance, capturing heteroscedastic aleatoric uncertainty.

Aleatoric uncertainty

Aleatoric uncertainty captures the inherent randomness in the data-generating process. It represents irreducible noise (e.g., measurement noise) that cannot be mitigated by collecting more data [36]. Aleatoric uncertainty can be homoscedastic, *i.e.* constant across the domain, or heteroscedastic, where noise varies with the input.

Widely adopted prognostics methods that assume homoscedastic uncertainty include Particle Filtering approaches [37]. In contrast, real transformer insulation degradation data exhibit heteroscedasticity driven by load fluctuations, thermal inertia, and operational variability.

In heteroscedastic regression, the modified B-PINN outputs both the predictive mean $\hat{u}(x, t; \boldsymbol{\theta})$ and an input-dependent variance $\sigma^2(x, t; \boldsymbol{\theta})$. Under a Gaussian likelihood, the log-likelihood per ground truth sample u , corresponding to the spatiotemporal coordinates (x, t) is defined as follows:

$$\log p(u | x, t; \boldsymbol{\theta}) = -\frac{1}{2} \log (2\pi \sigma^2(x, t; \boldsymbol{\theta})) - \frac{(u - \hat{u}(x, t; \boldsymbol{\theta}))^2}{2\sigma^2(x, t; \boldsymbol{\theta})}. \quad (16)$$

During Monte Carlo inference (cf. Algorithm 2), the aleatoric uncertainty is estimated by averaging the predictive variance across the K posterior samples:

$$\widehat{\text{AU}}(x, t) = \frac{1}{K} \sum_{k=1}^K \sigma^2(x, t; \boldsymbol{\theta}_k) \quad (17)$$

where $\sigma^2(x, t; \boldsymbol{\theta}_k)$ is the network's variance output for parameter sample $\boldsymbol{\theta}_k$.

Epistemic uncertainty

Epistemic uncertainty represents uncertainty in the model parameters due to limited data or incomplete knowledge of the underlying system. Unlike aleatoric uncertainty, epistemic uncertainty is reducible with more informative data or stronger priors [38].

Bayesian PINNs quantify epistemic uncertainty by sampling from the variational posterior $q(\boldsymbol{\theta})$. With K total samples, epistemic uncertainty is estimated as the predictive variance across the Monte Carlo forward passes:

$$\widehat{\text{EU}}(x, t) = \frac{1}{K} \sum_{k=1}^K \hat{u}(x, t; \boldsymbol{\theta}_k)^2 - \left(\frac{1}{K} \sum_{k=1}^K \hat{u}(x, t; \boldsymbol{\theta}_k) \right)^2 \quad (18)$$

where $\hat{u}(x, t; \theta_k)$ is the model prediction using parameter sample θ_k .

Total predictive uncertainty

Using variance as the uncertainty metric, the total predictive uncertainty can be decomposed using the law of total variance [39]:

$$\sigma^2(u|x) = \underbrace{\sigma_\theta^2[E_{u|x,\theta}(u|x, \theta)]}_{\text{epistemic}} + \underbrace{E_\theta[\sigma_{u|x,\theta}^2(u|x, \theta)]}_{\text{aleatoric}} \quad (19)$$

where $\sigma_\theta^2[E_{u|x,\theta}(u|x, \theta)]$ represents the epistemic uncertainty and $E_\theta[\sigma_{u|x,\theta}^2(u|x, \theta)]$ represents the aleatoric uncertainty.

B-PINNs Training with Total Uncertainty Quantification

In the B-PINN setting without aleatoric heteroscedastic uncertainty, the loss in Eq. (11) is minimized to estimate the variational posterior. In order to incorporate the heteroscedastic uncertainty, the Gaussian heteroscedastic log-likelihood in Eq. (16) is adopted, where the contribution of a spatio-temporal data point (x, t) to the expected negative log-likelihood is defined as follows:

$$\text{NLL}_{\text{hetero}}(x, t; \theta) = \frac{1}{2} \log(2\pi\sigma_u^2(x, t; \theta)) + \frac{(u - \mu_{\hat{u}}(x, t; \theta))^2}{2\sigma_u^2(x, t; \theta)} \quad (20)$$

where u is the solution or ground truth, $\mu_{\hat{u}}(x, t; \theta)$ is the mean value of the solution, and $\sigma_u^2(x, t; \theta)$ is the variance of the solution calculated from the proposed B-PINN architecture (cf. Figure 1).

When VI is used to approximate the posterior distribution, the NLL terms associated with the initial conditions, boundary conditions, and residuals are incorporated into the ELBO. Each contribution is scaled by its corresponding weighting coefficient λ . In practice, the optimization is formulated as a minimization problem [cf. Eq. (11)]. Consequently, the per-sample Monte Carlo training objective corresponds to minimizing the variational free energy, obtained by combining the KL divergence term with the weighted NLL components. The resulting loss function used during training is given by:

$$\begin{aligned} \mathcal{L}^{(k)} = & \log q(\theta^{(k)} | \phi) - \log p(\theta^{(k)}) \\ & + \lambda_0 \text{NLL}_{\text{hetero}}^{(0)}(\theta^{(k)}) + \lambda_b \text{NLL}_{\text{hetero}}^{(\text{bc})}(\theta^{(k)}) + \lambda_r \text{NLL}_{\text{hetero}}^{(r)}(\theta^{(k)}) \end{aligned} \quad (21)$$

where each $\text{NLL}_{\text{hetero}}^{(.)}(\theta^{(k)})$ term is the sum over the corresponding initial condition, boundary condition and residual points of Eq. (20).

Algorithm 1 summarizes the total predictive uncertainty inference process for B-PINNs.

Algorithm 1 Total predictive uncertainty inference for Bayesian PINNs.

```

1: Input: B-PINN model  $f(x, t; \theta)$ , test location  $(x, t)$ , posterior samples  $\{\theta_k\}_{k=1}^K$ 
2: for  $k = 1$  to  $K$  do
3:    $[\mu_{\hat{u}}, \sigma_{\hat{u}}^2] = f(x, t; \theta)$  ▷ Predictive mean and aleatoric variance
4:   Store  $\mu_{\hat{u}}$  in vector  $\vec{u}$ 
5:   Store  $\sigma_{\hat{u}}^2$  in vector  $\vec{\sigma}^2$ 
6: end for
7:  $\hat{u}(x, t) \leftarrow \frac{1}{K} \sum_k \vec{u}_k$ 
8:  $\widehat{\text{EU}}(x, t) \leftarrow \frac{1}{K} \sum_k \vec{u}_k^2 - \hat{u}(x, t)^2$ 
9:  $\widehat{\text{AU}}(x, t) \leftarrow \frac{1}{K} \sum_k \vec{\sigma}_k$ 
10:  $\sigma_{\text{TU}}(x, t) = \widehat{\text{EU}}(x, t) + \widehat{\text{AU}}(x, t)$ 
11: return  $\hat{u}(x, t), \sigma_{\text{TU}}(x, t)$ 

```

3 Experiments

The case study examines the lifetime of a distribution transformer installed in a floating solar power plant in Spain [14]. Details of the distribution transformer are summarized in Appendix A.4.

The dataset was preprocessed by removing variables without measurements, duplicate entries, and incorrect sensor readings. Missing values were imputed with average values. Figure 3 shows the available minutely sampled time series for ambient temperature, oil temperature, and load with a total of 5760 samples over 4 days of operation. Oil and winding temperature profiles analysed in this study are based on this minute-level sampling.

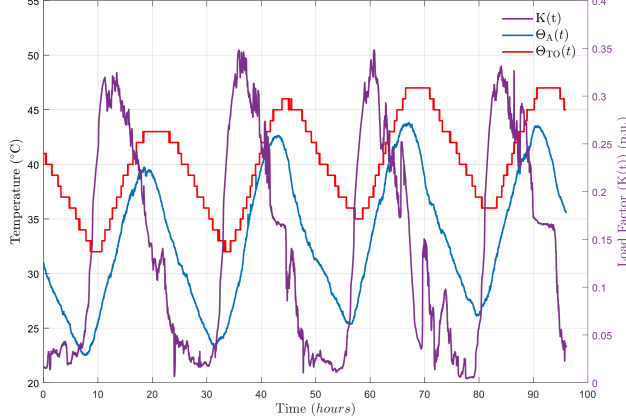


Figure 3: Distribution transformer load (K), ambient temperature (Θ_A), and top-oil temperature (Θ_{TO}) over four days of operation with one-minute resolution, operated at a floating photovoltaic substation.

Figure 4 shows the numerical solution of Eqs. (22)–(25), solved using finite element method (FEM) with Matlab’s pdepe solver [40]. The solution is experimentally validated against fiber optic sensor measurements installed at different transformer heights. Refer to [17] for more details.

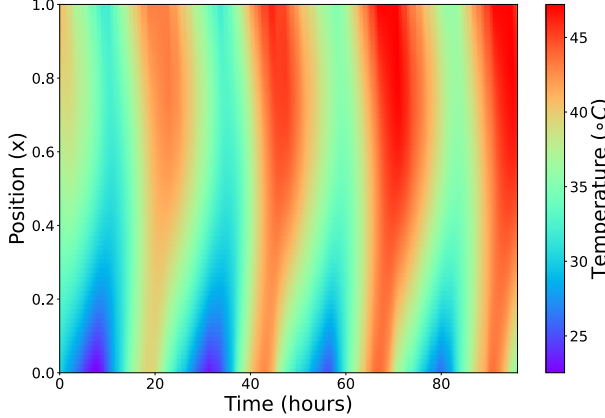


Figure 4: Spatiotemporal transformer oil temperature estimation obtained through a finite element method using the data in Figure 3 and the heat-diffusion 1D partial differential equation defined in Appendix A.

3.1 Setup

The implemented B-PINN configuration uses two layers with 50 neurons each, and Laplace prior distribution. An extensive hyperparameter study and justification of the selected parameters can be found in [30]. The influence of the number of boundary condition points, initial points, and residual points is further evaluated in Subsection 3.3 to determine their influence on the accuracy and uncertainty of the solution. For the homoscedastic B-PINN configuration, input data and residual data variance follow $\sigma_i = \mathcal{N}(0, 0.01)$ and $\sigma_r = \mathcal{N}(0, 0.01)$.

All experiments use VI to approximate the posterior distribution. Each simulation is repeated five times for numerical stability, and mean and standard deviation values are reported. All models are implemented from scratch using Tensor-

Flow Probability. The optimization algorithm is Adam, with a learning rate of 0.01 and a batch size of 16. All B-PINN models are trained for 15000 epochs, with early stopping applied using a patience of 200 epochs. The weights of the individual loss terms have been manually weighted, with final values of $\lambda_0=1$, $\lambda_b=1$, and $\lambda_r=10^{-4}$.

The vanilla PINN model is implemented using the Adam optimization algorithm for the first 20000 iterations, followed by the L-BFGS optimizer for the last 10000 iterations. The terms of individual loss terms have been manually weighted with final values of $\lambda_0=1$, $\lambda_b=1$, and $\lambda_r=10^{-6}$. Finally, the d-PINN model is designed taking the vanilla PINN architecture as the reference model, including additional dropout layers. The dropout rate is tested for a range of values $\rho=[0.05, 0.1, 0.15, 0.2, 0.25]$, with $K=200$ Monte Carlo iterations. Further details of the benchmarking models are provided in Appendix B.

3.2 Results

Comparative Results

Five main configurations are evaluated in this study: (a) B-PINN with total uncertainty quantification (epistemic and heteroscedastic aleatoric uncertainty), (b) d-PINN with total uncertainty quantification (epistemic and heteroscedastic aleatoric uncertainty), (c) B-PINN with epistemic uncertainty and homoscedastic aleatoric noise, (d) d-PINN with epistemic uncertainty and homoscedastic aleatoric noise, and (e) vanilla deterministic PINN without uncertainty quantification.

Configurations (a) and (b) enable a direct comparison of total UQ capabilities between B-PINN and d-PINN. The impact of modelling heteroscedastic aleatoric uncertainty is subsequently analysed by comparing configurations (a) and (b) with their homoscedastic counterparts (c) and (d). The vanilla PINN serves as a deterministic baseline for completeness.

Table 2 reports the probabilistic performance metrics (defined in Appendix B) across different prediction instants for all considered configurations, including continuously ranked probability score (CRPS) and negative log-likelihood (NLL), along with root-mean-square error (RMSE). Overall, the heteroscedastic B-PINN achieves the best performance across all metrics and time instants. In particular, it achieves a total RMSE of 1.09, corresponding to a 57.3% improvement over the vanilla PINN. When compared with the heteroscedastic d-PINN, the B-PINN yields a 42.6% reduction in RMSE and a 40.2% improvement in CRPS, highlighting its superior uncertainty calibration and predictive accuracy.

Table 2: Comparison of probabilistic performance results for different prediction instants across different B-PINN and d-PINN models with heteroscedastic and homoscedastic UQ, along with epistemic UQ. For completeness, vanilla PINN results are also reported. Values reported as mean \pm std, best results highlighted.

Instant [h]	Heteroscedastic UQ						Homoscedastic UQ						Vanilla PINN	
	B-PINN			d-PINN			B-PINN			d-PINN				
	RMSE(\downarrow)	CRPS(\downarrow)	NLL(\downarrow)	RMSE(\downarrow)	CRPS(\downarrow)	NLL(\downarrow)	RMSE(\downarrow)	CRPS(\downarrow)	NLL(\downarrow)	RMSE(\downarrow)	CRPS(\downarrow)	NLL(\downarrow)		
0	0.03 \pm 0.02	0.03 \pm 0.01	-1.25 \pm 0.45	0.14 \pm 0.00	0.23 \pm 0.02	0.84 \pm 0.06	0.02 \pm 0.01	0.12 \pm 0.08	0.16 \pm 0.69	0.20 \pm 0.02	0.38 \pm 0.01	1.38 \pm 0.02	1.47	
3	0.31 \pm 0.04	0.19 \pm 0.01	0.41 \pm 0.65	1.65 \pm 0.25	0.96 \pm 0.12	1.92 \pm 0.01	0.33 \pm 0.12	0.20 \pm 0.09	0.40 \pm 0.54	1.77 \pm 0.14	1.06 \pm 0.10	2.00 \pm 0.10	1.45	
6	0.32 \pm 0.04	0.21 \pm 0.04	1.61 \pm 1.43	2.15 \pm 0.31	1.24 \pm 0.18	2.13 \pm 0.05	0.30 \pm 0.01	0.20 \pm 0.03	0.49 \pm 0.33	1.86 \pm 0.20	1.13 \pm 0.14	2.07 \pm 0.15	2.17	
18	0.34 \pm 0.01	0.22 \pm 0.01	0.63 \pm 0.12	1.30 \pm 0.06	0.88 \pm 0.15	1.94 \pm 0.36	0.67 \pm 0.39	0.41 \pm 0.23	1.07 \pm 0.57	1.16 \pm 0.81	0.61 \pm 0.32	1.59 \pm 0.28	3.29	
25	0.42 \pm 0.02	0.26 \pm 0.02	0.93 \pm 0.09	2.04 \pm 0.47	1.18 \pm 0.31	2.12 \pm 0.37	0.57 \pm 0.05	0.35 \pm 0.05	1.39 \pm 0.71	1.81 \pm 0.11	1.07 \pm 0.07	2.01 \pm 0.07	1.78	
50	0.45 \pm 0.13	0.28 \pm 0.08	0.72 \pm 0.28	3.35 \pm 0.58	2.06 \pm 0.51	2.76 \pm 0.45	1.07 \pm 0.83	0.71 \pm 0.58	2.06 \pm 1.33	3.47 \pm 0.79	0.89 \pm 0.43	1.86 \pm 0.36	2.27	
Total	1.09 \pm 0.21	0.58 \pm 0.09	1.75 \pm 0.19	1.90 \pm 0.57	0.97 \pm 0.36	1.80 \pm 0.45	1.12 \pm 0.47	0.66 \pm 0.23	1.98 \pm 0.73	1.96 \pm 0.13	1.10 \pm 0.06	2.10 \pm 0.07	2.55	

The heteroscedastic B-PINN formulation consistently outperforms its homoscedastic counterpart across different prediction instants. While total RMSE values remain comparable between both variants, remarkable improvements are observed in CRPS, indicating better calibrated predictive distributions when heteroscedastic uncertainty is modelled. Although the homoscedastic B-PINN achieves slightly lower NLL values at specific instants (e.g., $t = 6$ h), the heteroscedastic B-PINN yields an overall NLL improvement of 11.6%. At early instants, the heteroscedastic B-PINN achieves near-zero errors, while maintaining stable performance as the prediction instant increases.

In contrast, d-PINN exhibit significantly degraded performance, particularly at longer horizons. For instance, at $t = 50$ h, the heteroscedastic d-PINN reaches an RMSE of 3.35, representing a 645% increase relative to the heteroscedastic B-PINN. This degradation reflects reduced predictive accuracy and over-dispersed uncertainty estimates, underscoring the limitations of dropout-based uncertainty approximation in the analysed setting.

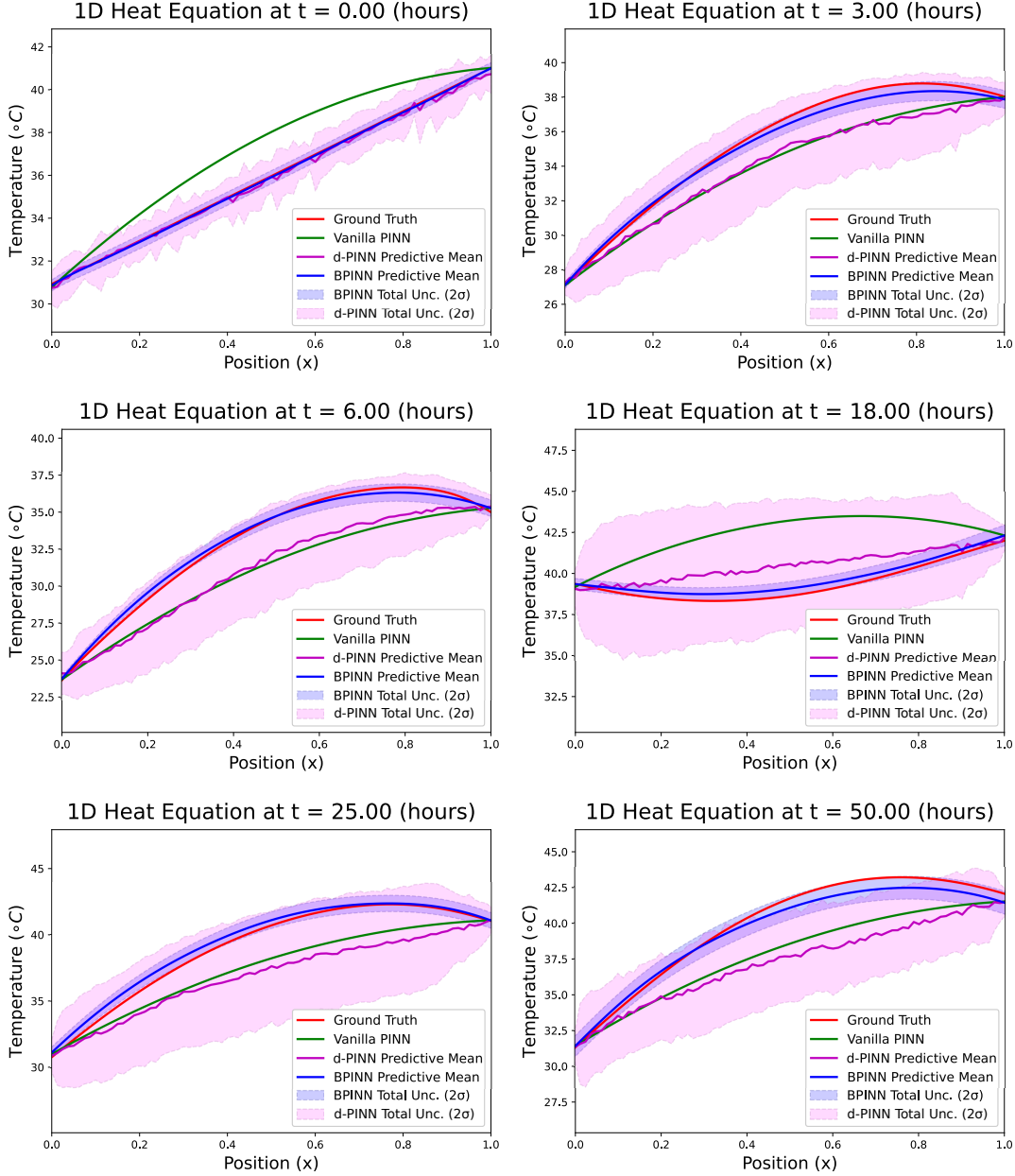


Figure 5: Spatiotemporal transformer insulation oil temperature estimates at different time instants for heteroscedastic B-PINN, heteroscedastic d-PINN, and vanilla PINN models, along with the corresponding measured ground truth values.

Figure 5 illustrates the spatiotemporal transformer insulation oil temperature predictions at selected time instants for the heteroscedastic B-PINN, heteroscedastic d-PINN, and vanilla PINN models, together with the measured ground truth.

Among the heteroscedastic models, the total predictive uncertainty produced by the d-PINN is consistently wider than that of the B-PINN across all considered time instants and spatial locations. This behavior reflects the approximate nature of Monte Carlo dropout, which tends to generate overly conservative epistemic uncertainty estimates, particularly in regions with limited data support or during extrapolation [30].

In contrast, the B-PINN yields tighter and more structured uncertainty bands while maintaining closer agreement between the predictive mean and the ground truth temperature profiles. The predictive mean of the d-PINN closely

follows that of the vanilla PINN, with small but systematic deviations from the measured values. This indicates that dropout-based uncertainty quantification primarily affects the dispersion of predictions rather than substantially correcting the bias of the underlying deterministic solution. Overall, these results highlight the advantages of fully Bayesian inference in B-PINNs for achieving a more balanced trade-off between predictive accuracy and uncertainty sharpness.

Uncertainty Assessment

Focusing on the homoscedastic and heteroscedastic B-PINN configurations that incorporate epistemic uncertainty, Table 3 displays uncertainty-specific metrics that quantify both calibration and sharpness. Calibration reflects the agreement between empirical coverage and nominal confidence levels, measured through the miscalibration area, while sharpness characterizes the concentration of the predictive distributions independently of calibration.

Table 3: Comparison of calibration and sharpness metrics for homoscedastic and heteroscedastic B-PINN models evaluated across the operational days shown in Figure 3.

Metric	B-PINN Heteroscedastic	B-PINN Homoscedastic
Miscalibration area	0.1956 ± 0.1616	0.2135 ± 0.0591
Sharpness	0.5258 ± 0.3369	0.5603 ± 0.0892

From Table 3, it can be observed that the heteroscedastic B-PINN achieves a slightly lower miscalibration area compared with the homoscedastic configuration, indicating marginally improved calibration of the predictive uncertainty. This suggests that allowing the aleatoric variance to depend on the input data enables the B-PINN to better adapt uncertainty levels across the spatiotemporal domain.

In terms of sharpness, the heteroscedastic B-PINN produces slightly sharper predictive distributions on average, but with increased variability. This reflects localized increases in uncertainty within regions characterized by higher model uncertainty or data uncertainty. Overall, these results highlight the inherent trade-off between calibration and sharpness and demonstrate that heteroscedastic modeling provides a more flexible and expressive uncertainty representation when combined with epistemic uncertainty in Bayesian PINNs.

Taking the heteroscedastic B-PINN model, in order to directly compare the relative contribution of epistemic and aleatoric sources of uncertainty, the daily influence of each uncertainty component is quantified. Figure 6 illustrates the joint probability density of aleatoric and epistemic uncertainty for four representative days. It can be observed that, for all considered days, the highest-density regions are concentrated around well-defined modes in the joint aleatoric–epistemic uncertainty space, indicating stable dominant uncertainty regimes. Across all days, epistemic uncertainty spans approximately the range $\langle 0.0015, 0.004 \rangle$, while aleatoric uncertainty varies over a wider interval of approximately $\langle 0.10, 0.22 \rangle$, reflecting the input-dependent nature of the heteroscedastic noise model.

The spread of the epistemic uncertainty exhibits noticeable day-to-day variability, with the largest dispersion observed on Day 3, suggesting increased model uncertainty likely associated with reduced data support or higher physical model mismatch. Conversely, the aleatoric uncertainty shows its largest variability on Day 4, indicating stronger input-dependent noise effects for that operating condition.

As for the density concentration, the compact high-density regions indicate that most uncertainty realizations are confined to narrow aleatoric–epistemic regimes, while the extended tails reflect occasional excursions into higher uncertainty states. This joint representation highlights the complementary roles of epistemic and aleatoric uncertainty and enables a direct assessment of their relative magnitude and interaction over time.

In order to further compare the relative contributions of epistemic and heteroscedastic aleatoric sources of uncertainty, the influence of each uncertainty component is quantified separately. Figure 7 illustrates the measured ground truth, vanilla PINN output, and the proposed B-PINN mean and standard deviation predictions, along with the aleatoric and epistemic uncertainty estimates calculated by the B-PINN for the instant $t = 25$.

It can be observed from Figure 7 that, in the homoscedastic B-PINN configuration, the aleatoric uncertainty remains spatially constant, reflecting the assumption of input-independent observation noise. As a result, the total predictive uncertainty exhibits a nearly uniform contribution from the aleatoric component across the spatial domain.

In contrast, the heteroscedastic B-PINN configuration learns an input-dependent aleatoric uncertainty, which adapts to variations in temperature. This input data leads to spatially varying uncertainty bands that more closely follow the underlying solution structure. Consequently, the heteroscedastic model yields uncertainty bounds that are generally tighter in well-informed regions while allowing localized uncertainty increase where the model or data uncertainty

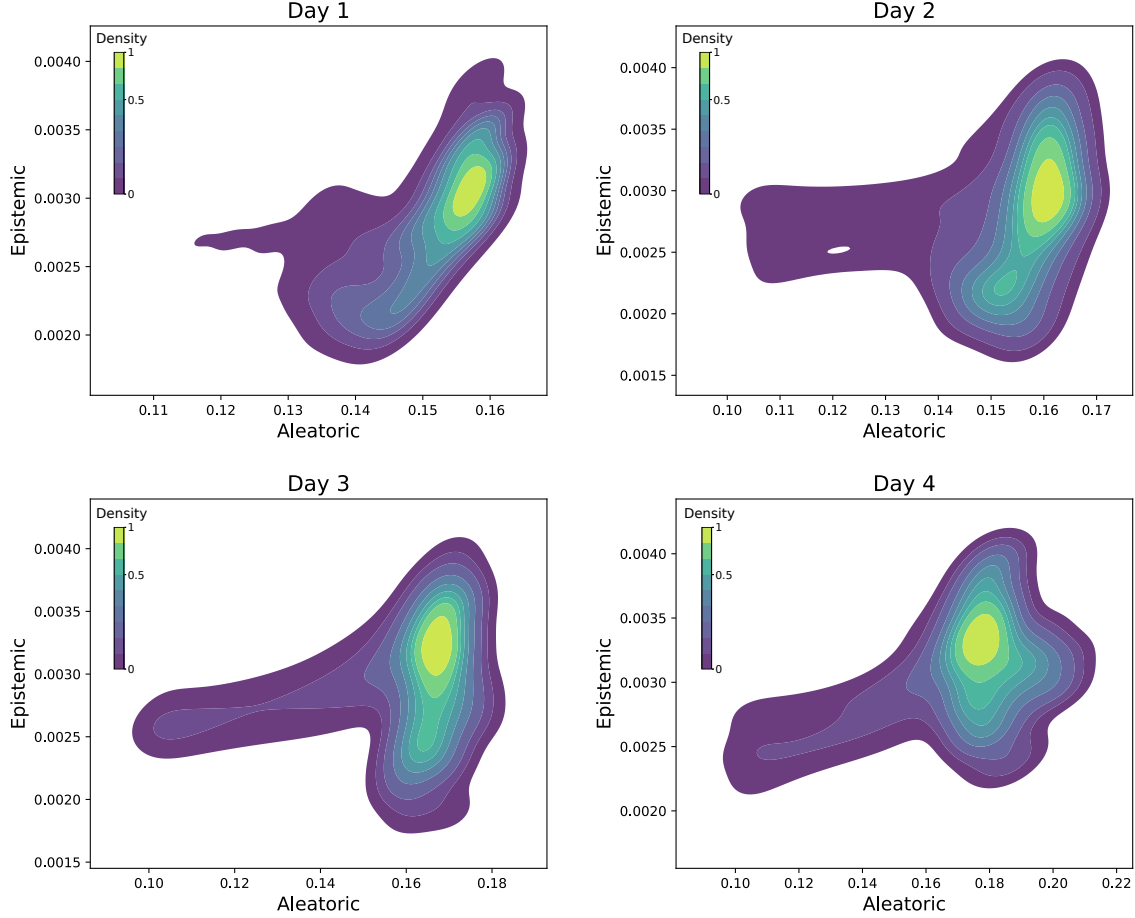


Figure 6: Joint probability density of aleatoric (heteroscedastic) and epistemic uncertainty estimated by the B-PINN model for four representative days. The color intensity indicates the relative density of uncertainty realizations, with brighter regions corresponding to higher probability mass.

is higher. This comparison illustrates the increased expressiveness and reduced over-conservatism of heteroscedastic uncertainty modeling within the B-PINN framework.

Ageing Prediction

Building on the spatiotemporal probabilistic temperature predictions obtained with the B-PINN and d-PINN models under total UQ, Figure 8 shows the resulting spatiotemporal insulation ageing estimates $p(\hat{V}(x, t))$. For each model,

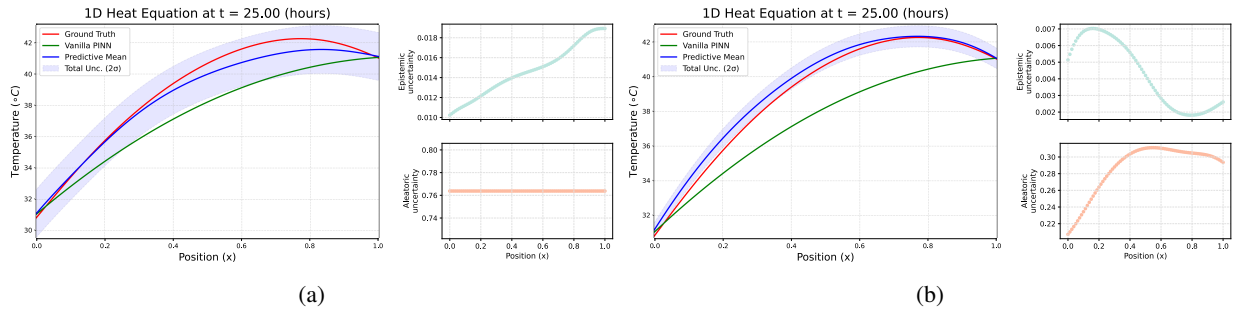


Figure 7: Spatiotemporal temperature estimates at $t = 25$ hours with the corresponding decomposition into epistemic and aleatoric uncertainty. (a) B-PINN homoscedastic; (b) B-PINN heteroscedastic configuration.

the predictive mean and the associated standard deviation are shown (see Appendix A.3 for empirical ageing model details).

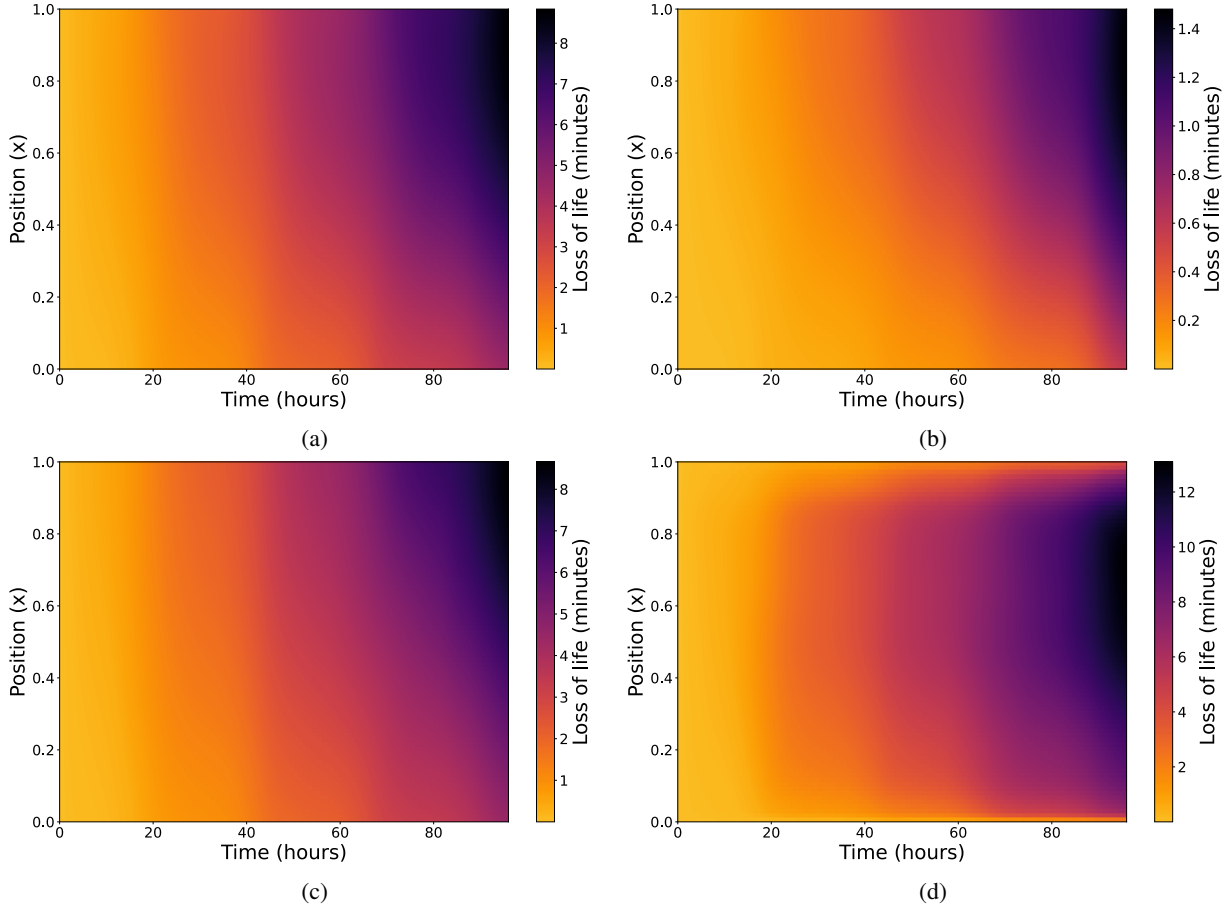


Figure 8: Probabilistic spatiotemporal ageing predictions for B-PINN and d-PINN models with total UQ: (a) mean estimate of B-PINN, (b) standard deviation of B-PINN, (c) mean estimate of d-PINN, and (d) standard deviation of d-PINN.

Figures 8(a) and (b) illustrate the mean and standard deviation of the ageing estimates obtained with the B-PINN, while Figures 8(c) and (d) show the corresponding results for the d-PINN. The predictive mean ageing estimates are broadly consistent across both models, with maximum accumulated ageing values of 8.83 minutes for the B-PINN and 8.65 minutes for the d-PINN. This indicates that, at the level of point estimates, both models capture similar expected ageing dynamics.

However, substantial differences emerge in the associated predictive uncertainty. The B-PINN exhibits a maximum ageing standard deviation of 1.48 minutes, whereas the d-PINN achieves a larger maximum standard deviation of 13.09 minutes. This discrepancy reflects the significantly higher uncertainty propagated by the dropout-based approximation, particularly when integrated over space and time. In this regime, the standard deviation of the d-PINN ageing estimate exceeds the corresponding mean value, indicating a loss of informative predictive content and limited practical interpretability.

The differences between Figure 8(c) and (d) highlight the critical impact of uncertainty modeling choices in prognostics applications. The wider uncertainty bands produced by the d-PINN indicate a tendency toward overly conservative ageing estimates. When employed in maintenance and asset management decision-making, such uncertainty may lead to premature asset replacement, even in scenarios where the expected ageing remains moderate.

To further assess the accuracy and calibration of the ageing predictions, FEM-based transformer oil temperature estimates (Figure 4) are used as ground truth to compute the corresponding spatiotemporal insulation ageing profiles. Based on this reference, ageing prediction errors are evaluated for the B-PINN and d-PINN models with respect to

the estimates shown in Figure 8. Figure 9 shows the resulting mean ageing estimation error fields, with contour lines indicating the standard deviation of the error.

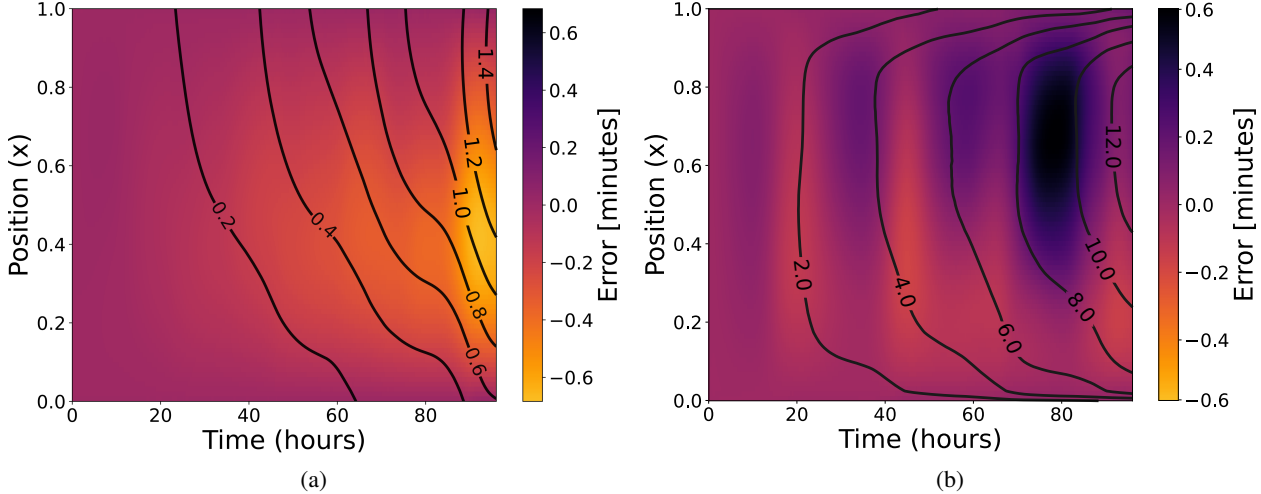


Figure 9: Spatio-temporal temperature prediction errors for (a) B-PINN and (b) d-PINN. The heatmap shows the mean error relative to FEM. The contour lines indicate the standard deviation of the error.

The results show that the variance of the ageing estimation error for the d-PINN grows substantially faster (approximately an order of magnitude faster) than that of the B-PINN. Such rapidly expanding uncertainty directly affects decision-making confidence, as excessively diffuse error bounds hinder reliable risk assessment and RUL evaluation. In contrast, the B-PINN maintains a more controlled and balanced growth of uncertainty alongside the ageing estimation error, resulting in more reliable probabilistic prognostic outputs.

3.3 Sensitivity Assessment

Figure 10 shows probabilistic metrics for the heteroscedastic B-PINN approach, keeping the network architecture and prior assumptions fixed, evaluated over multiple realizations. These results summarize the impact of different sampling strategies on UQ performance by varying the number of initial condition samples (N_i), physics residual collocation points (N_r), and boundary condition samples (N_b). The selected configurations span sparse to moderately dense initial sampling ($N_i = \{5, 100, 200\}$), progressively increasing physics residual enforcement ($N_r = \{5000, 10000, 20000\}$), and increasing levels of boundary conditions coverage ($N_b = \{2880, 5760, 8640, 11520\}$) covering 25%, 50%, 75%, and 100% available samples for the upper and lower BCs, thereby enabling a systematic analysis of how data availability and physics constraints jointly influence probabilistic prediction quality.

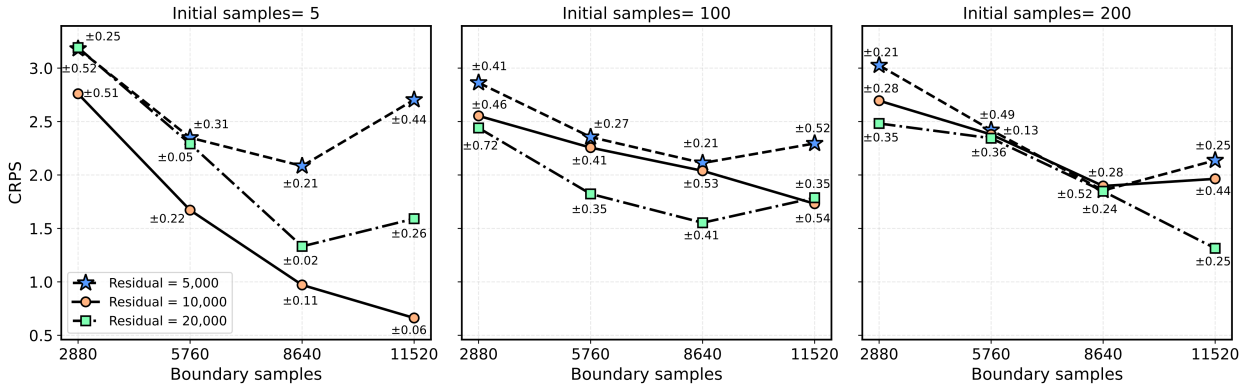


Figure 10: Sensitivity analysis of the CRPS metric with respect to the number of boundary condition samples, initial samples and residual samples. Markers indicate the mean, with annotations representing the corresponding std of the CRPS metric across runs. Lower CRPS values indicate improved UQ performance.

Focusing on the CRPS, Figure 10 shows that probabilistic performance is primarily governed by the number of residual collocation points rather than by the number of initial condition samples. Across all configurations, the lowest CRPS values are consistently achieved with a moderate number of residual samples (10000), indicating an effective balance between physics enforcement and the model’s ability to adapt uncertainty. Increasing the number of residual points beyond this level tends to worsen CRPS, suggesting that overly dense physics constraints can restrict the flexibility of the model and lead to less well-calibrated predictions. In contrast, increasing the number of initial samples from 5 to 200 does not produce systematic improvements in CRPS, indicating that the initial state is already sufficiently constrained with only a few samples. Finally, boundary condition enforcement consistently yields lowest CRPS values when all 11520 samples are used, emphasizing the stabilizing influence of boundary information on predictive accuracy and uncertainty sharpness.

The observed CRPS trends can be directly interpreted through the interplay between epistemic and aleatoric uncertainty components in the heteroscedastic B-PINN. CRPS penalizes both miscalibration and excessive dispersion, and therefore reflects the balance between epistemic and aleatoric uncertainty. When the number of residual collocation points is too small (5000), insufficient physics enforcement leads to increased epistemic uncertainty and broader predictive distributions, resulting in higher CRPS values. Conversely, excessively dense residual sampling (20000) over-constrains the solution, suppressing epistemic uncertainty, but inducing amplified aleatoric uncertainty, which again degrades CRPS.

The lowest CRPS values are consistently obtained for a moderate number of residual samples (10000), corresponding to a regime in which epistemic uncertainty is effectively reduced through physics-informed regularization, while retaining sufficient flexibility for input-dependent aleatoric uncertainty to be expressed. A similar interpretation applies to boundary condition sampling: full boundary enforcement (11520) stabilizes the solution near domain boundaries, reducing epistemic uncertainty leakage and preventing artificial increases of aleatoric uncertainty, thereby improving CRPS. In contrast, reducing boundary samples increases epistemic uncertainty near the boundaries, which propagates into wider predictive distributions and higher CRPS values.

Finally, increasing the number of initial condition samples beyond a minimal sufficient level does not systematically improve CRPS, indicating that, for the analysed problem, epistemic uncertainty associated with the initial condition is already well constrained in low N_i regimes. Additional initial samples therefore contribute marginally to uncertainty reduction while potentially reducing the ability of the model to adapt aleatoric uncertainty, worsening the probabilistic performance.

4 Conclusion

Scientific Machine Learning (SciML) integrates physical knowledge with machine learning (ML), yielding predictive models that generalize more robustly than purely data-driven approaches while requiring less data. Hybrid Prognostics and Health Management (PHM) methods share conceptual similarities with SciML, as both combine physics-of-failure models with data-driven components. However, SciML provides a more principled learning framework in which physical constraints are embedded directly into the training process. To the best of the authors’ knowledge, this paradigm has not yet been fully explored within PHM in general, and for insulation material prognostics tasks in particular.

This work proposes a heteroscedastic Bayesian Physics-Informed Neural Network (B-PINN) framework for probabilistic insulation ageing estimation in electrical transformers, explicitly capturing epistemic and aleatoric sources of uncertainty. The proposed approach embeds the heat diffusion partial differential equation into the learning process while leveraging operational measurements of transformer loading and temperature. Epistemic uncertainty is represented by modeling Neural Network weights probabilistically, whereas heteroscedastic aleatoric uncertainty is learned through an input-dependent noise model enabled by architectural and training modifications to the B-PINN formulation.

Numerical experiments demonstrate that the proposed heteroscedastic B-PINNs consistently outperforms its homoscedastic counterpart across the evaluated configurations, yielding improved predictive accuracy, better-calibrated uncertainty estimates, and enhanced reliability. In terms of sharpness, the heteroscedastic B-PINN produces, on average, sharper predictive distributions, albeit with increased variability associated with localized adaptations to input-dependent uncertainty. In contrast, heteroscedastic dropout PINNs (d-PINNs) exhibit degraded performance, characterized by reduced predictive accuracy and systematically over-dispersed uncertainty estimates, particularly at long prediction instants.

A detailed decomposition of aleatoric and epistemic uncertainty in the heteroscedastic B-PINN configuration shows that most uncertainty realizations remain concentrated within narrow aleatoric–epistemic regimes, indicating stable

uncertainty behavior. Occasional extended tails correspond to transient periods of data scarcity or localized model mismatch.

From a prognostics perspective, the resulting ageing estimates confirm that the heteroscedastic B-PINN provides the most reliable and informative predictions. Conversely, the heteroscedastic d-PINN yields broad uncertainty bounds that hinder maintenance decision-making and may lead to overly conservative asset replacement strategies.

A sensitivity analysis of the heteroscedastic B-PINN with respect to the number of initial condition, boundary condition, and residual collocation points, further provides practical insights into the configuration of B-PINNs for prognostics applications. For the analyzed case study: (i) a moderate number of residual collocation points yields optimal Continuous Ranked Probability Score (CRPS) values, reflecting a balanced trade-off between physics enforcement and uncertainty adaptability; (ii) the influence of initial condition samples is limited when the initial state is sufficiently constrained; and (iii) full boundary condition enforcement leads to the best CRPS performance, highlighting the stabilizing role of boundary information in both predictive accuracy and uncertainty sharpness.

Beyond methodological contributions, the proposed heteroscedastic B-PINN framework offers tangible benefits for transformer asset management. By explicitly quantifying and propagating epistemic and aleatoric uncertainty, the approach supports informed decision-making under data scarcity and localized model mismatch, mitigating the risks associated with overly conservative or unsafe maintenance strategies.

The present implementation relies on variational inference for posterior approximation. Future work will explore alternative Bayesian inference techniques and physics-informed priors, to further enhance uncertainty quantification and robustness in SciML-based PHM frameworks.

Acknowledgements

This work has been partially funded by the Spanish State Research Agency (grant No. PID2024-156284OA-I00) and the Basque Government (grants IT1504-22, KK-2024/00030). Jose I. Aizpurua is funded by the Ramón y Cajal Fellowship, Spanish State Research Agency (grant No. RYC2022-037300-I), co-funded by MCIU/AEI/10.13039/501100011033 and FSE+.

Conflict of Interest

The authors declare no conflict of interest.

References

- [1] G. J. Vachtsevanos, F. Lewis, M. Roemer, A. Hess, B. Wu, *Intelligent fault diagnosis and prognosis for engineering systems*, volume 456, Wiley Online Library, **2006**.
- [2] M. Kordestani, M. Saif, M. E. Orchard, R. Razavi-Far, K. Khorasani, *IEEE Transactions on Reliability* **2021**, *70*, 2 728.
- [3] G. E. Karniadakis, I. G. Kevrekidis, L. Lu, P. Perdikaris, S. Wang, L. Yang, *Nature Reviews Physics* **2021**, *3*, 6 422.
- [4] M. Raissi, P. Perdikaris, G. Karniadakis, *Journal of Computational Physics* **2019**, 378 686.
- [5] N. Kovachki, Z. Li, B. Liu, K. Azizzadenesheli, K. Bhattacharya, A. Stuart, A. Anandkumar, *J. Mach. Learn. Res.* **2023**, *24*, 1.
- [6] Z. Li, H. Zheng, N. Kovachki, D. Jin, H. Chen, B. Liu, K. Azizzadenesheli, A. Anandkumar, *ACM / IMS J. Data Sci.* **2024**, *1*, 3.
- [7] Z. Liu, Y. Wang, S. Vaidya, F. Ruehle, J. Halverson, M. Soljačić, T. Y. Hou, M. Tegmark, In *International Conference on Learning Representations (ICLR)*. **2025** .
- [8] J. D. Toscano, V. Oommen, A. J. Varghese, Z. Zou, N. A. Daryakenari, C. Wu, G. E. Karniadakis, *Mach. Learn. Comput. Sci. Eng.* **2025**, *1*, 15.
- [9] J. I. Aizpurua, V. M. Catterson, In *Annual Conference of the PHM Society*, volume 7. **2015** .
- [10] J. Guo, Z. Li, M. Li, *IEEE Transactions on Reliability* **2020**, *69*, 3 1110.
- [11] E. Zio, *Reliability Engineering & System Safety* **2022**, 218 108119.
- [12] M. Arias Chao, C. Kulkarni, K. Goebel, O. Fink, *Reliability Engineering & System Safety* **2022**, 217 107961.
- [13] M. Daigle, I. Roychoudhury, A. Bregon, In *Annual Conference of the PHM Society*, volume 7. **2015** .

[14] J. I. Aizpurua, I. Ramirez, I. Las, L. d. Rio, A. Ortiz, B. G. Stewart, *IEEE Trans. Pow. Del.* **2023**, 38, 1 599.

[15] J. Alcibar, J. I. Aizpurua, E. Zugasti, O. Peñagarikano, *Engineering Applications of Artificial Intelligence* **2025**, 146 110246.

[16] F. Wang, Z. Zhai, Z. Zhao, Y. Di, X. Chen, *Nature Communications* **2024**, 15, 1 4332.

[17] I. Ramirez, J. Pino, D. Pardo, M. Sanz, L. del Rio, A. Ortiz, K. Morozovska, J. I. Aizpurua, *Engineering Applications of Artificial Intelligence* **2025**, 139 109556.

[18] S. Sankararaman, *Mechanical Systems and Signal Processing* **2015**, 52 228.

[19] M. Salinas-Camus, K. Goebel, N. Eleftheroglou, *Mechanical Systems and Signal Processing* **2025**, 237 113015.

[20] K. Linka, A. Schäfer, X. Meng, Z. Zou, G. E. Karniadakis, E. Kuhl, *Computer Methods in Applied Mechanics and Engineering* **2022**, 402 115346.

[21] J. Li, X. Long, X. Deng, W. Jiang, K. Zhou, C. Jiang, X. Zhang, *Reliability Engineering & System Safety* **2024**, 245 109963.

[22] A. S. Nair, B. Jacob, A. A. Howard, J. Drgona, P. Stinis, E-pinns: Epistemic physics-informed neural networks, **2025**.

[23] L. Podina, M. T. Rad, M. Kohandel, In *ICLR 2024 Workshop on AI4Differential Equations In Science*. **2024** .

[24] D. Zhang, L. Lu, L. Guo, G. E. Karniadakis, *Journal of Computational Physics* **2019**, 397 108850.

[25] X. Jiang, X. Wang, Z. Wen, E. Li, H. Wang, *International Communications in Heat and Mass Transfer* **2023**, 147 106940.

[26] Z. Zou, Z. Wang, G. E. Karniadakis, *arXiv preprint arXiv:2503.06320* **2025**.

[27] E. Hüllermeier, W. Waegeman, *Machine learning* **2021**, 110, 3 457.

[28] J. Fernández, J. Chiachío, M. Chiachío, J. Barros, M. Corbetta, *Engineering Applications of Artificial Intelligence* **2023**, 119 105790.

[29] R. G. Nascimento, F. A. Viana, M. Corbetta, C. S. Kulkarni, *Scientific Reports* **2023**, 13, 1 13856.

[30] I. Ramirez, J. Alcibar, J. Pino, M. Sanz, D. Pardo, J. I. Aizpurua, In *Annual Conference of the PHM Society*, volume 17. **2025** .

[31] J. Aizpurua, B. Stewart, S. McArthur, M. Penalba, M. Barrenetxea, E. Muxika, J. Ringwood, *Reliability Engineering & System Safety* **2022**, 226 108676.

[32] M. Raissi, P. Perdikaris, G. Karniadakis, *Journal of Computational Physics* **2019**, 378 686.

[33] L. G. Wright, T. Onodera, M. M. Stein, T. Wang, D. T. Schachter, Z. Hu, P. L. McMahon, *Nature* **2022**, 601, 7894 549.

[34] S. J. Anagnostopoulos, J. D. Toscano, N. Stergiopoulos, G. E. Karniadakis, *Computer Methods in Applied Mechanics and Engineering* **2024**, 421 116805.

[35] V. Fortuin, A. Garriga-Alonso, M. van der Wilk, L. Aitchison, *Software Impacts* **2021**, 9 100079.

[36] A. Kendall, Y. Gal, In I. Guyon, U. V. Luxburg, S. Bengio, H. Wallach, R. Fergus, S. Vishwanathan, R. Garnett, editors, *Advances in Neural Information Processing Systems*, volume 30. Curran Associates, Inc., **2017** 1–11.

[37] M. E. Orchard, G. J. Vachtsevanos, *Transactions of the Institute of Measurement and Control* **2009**, 31, 3-4 221.

[38] E. Hüllermeier, W. Waegeman, *Machine Learning* **2021**, 110, 3 457.

[39] S. Depeweg, J.-M. Hernandez-Lobato, F. Doshi-Velez, S. Udluft, In J. Dy, A. Krause, editors, *Proceedings of the 35th International Conference on Machine Learning*, volume 80 of *Proceedings of Machine Learning Research*. PMLR, **2018** 1184–1193.

[40] The MathWorks, Inc., *PDEPE Toolbox*, Natick, Massachusetts, USA, **2023**, URL <https://mathworks.com/>.

[41] International Electrotechnical Commission, *IEC 60076-7* **2018**.

[42] Y. Gal, Z. Ghahramani, In M. F. Balcan, K. Q. Weinberger, editors, *Proceedings of The 33rd International Conference on Machine Learning*, volume 48 of *Proceedings of Machine Learning Research*. PMLR, New York, New York, USA, **2016** 1050–1059.

[43] K. P. Murphy, *Machine learning: a probabilistic perspective*, MIT press, **2012**.

[44] C. M. Bishop, N. M. Nasrabadi, *Pattern recognition and machine learning*, volume 4, Springer, **2006**.

[45] M. Zamo, P. Naveau, *Mathematical Geosciences* **2018**, 50, 2 209.

[46] T. Gneiting, A. E. Raftery, A. H. Westveld, T. Goldman, *Monthly Weather Review* **2005**, 133, 5 1098.

A Transformer Thermal Model

Transformers are key assets for the reliable operation of the power grid. The increasing penetration of renewable energy sources to the grid affects the transformer's health [14]. The main insulating material for oil-immersed transformers is paper immersed oil, and their main failure mode is the insulation degradation. The insulating paper is made of cellulose polymer and the degree of polymerization determines the strength of the insulating paper [41]. The insulation paper degradation is directly caused by the thermal stress.

Accordingly, this section reviews the main transformer thermal modelling steps, including the oil temperature estimation stage (Section A.1) and subsequent winding temperature estimation stage, which is used to calculate the hottest-spot temperature (HST), *i.e.* highest insulation temperature (Section A.2). Finally, the thermal model is connected to the insulation aging assessment model, which is used to estimate the loss of life of the insulation (Section A.3).

A.1 Spatiotemporal Oil Temperature Modelling

The spatial distribution of oil and winding temperature is key for the cost-effective transformer health management. To capture this, a thermal modelling approach is developed based on partial differential equations (PDE). The heat diffusion PDE is considered to model the temporal and spatial evolution of the transformer oil temperature ($\Theta_O(x, t)$). Due to the transformer oil characteristics, radiative heat diffusion is considered and not convection. The general form of the one-dimensional heat diffusion equation is defined as [17]:

$$\begin{aligned} k \frac{\partial^2 \Theta_O(x, t)}{\partial x^2} + q(x, t) &= \rho c_p \frac{\partial \Theta_O(x, t)}{\partial t} \\ \frac{\partial^2 \Theta_O(x, t)}{\partial x^2} + \frac{1}{k} q(x, t) &= \frac{1}{\alpha} \frac{\partial \Theta_O(x, t)}{\partial t} \end{aligned} \quad (22)$$

where $x, t \in \mathbb{R}$ are the independent variables, which denote position [m] and time [s], respectively, $\Theta_O(x, t)$ is given in Kelvin [K], k is the thermal conductivity [W/m.K], c_p is the specific heat capacity [J/kg.K], ρ is the density [kg/m³], $q(x, t)$ is the rate of heat generation [W/m³], and $\alpha = \frac{k}{\rho c_p}$ is the thermal diffusivity [m²/s].

Figure 11 shows the thermal parameters of the transformer of the heat diffusion model, which considers the heat source, $q(x, t)$, and the convective heat transfer, $h(\Theta_O(x, t) - \Theta_A(t))$.

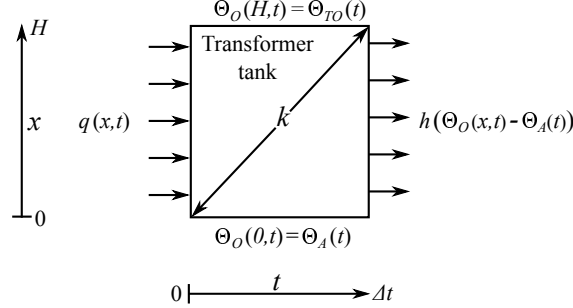


Figure 11: Transformer heat diffusion model [17].

The evolution of the heat source in space and time, $q(x, t)$, is defined as follows:

$$q(x, t) = P_0 + P_K(t) - h(\Theta_O(x, t) - \Theta_A(t)) \quad (23)$$

where $\Theta_A(t)$ is the ambient temperature, h is the convective heat transfer coefficient, P_0 is the no load losses [W], and $P_K(t)$ is the load losses, defined as follows:

$$P_K(t) = K(t)^2 \mu, \quad (24)$$

where $K(t)$ is the load factor [p.u.], and μ is the rated load losses [W].

The challenge is to accurately model the transformer oil temperature vertically along its height H (Figure 11). It can be observed that the spatial distribution is considered along the vertical axis (x). It is assumed that $\Theta_O(x, t)$ is equal

to $\Theta_A(t)$ at the bottom ($x=0$) and $\Theta_{TO}(t)$ at the top ($x=H$). Namely, these are the Dirichlet boundary conditions of the PDE that is going to be solved:

$$\begin{aligned}\Theta_O(0, t) &= \Theta_A(t) \\ \Theta_O(H, t) &= \Theta_{TO}(t)\end{aligned}\quad (25)$$

A.2 Hotspot Temperature (HST) Modelling

The HST is the most critical thermal indicator. However, direct measurements are difficult and expensive. Generally the HST value, $\Theta_H(t)$, is estimated indirectly from the top-oil temperature (TOT), $\Theta_{TO}(t)$, defined as [41]:

$$\Theta_H(t) = \Theta_{TO}(t) + \Delta\Theta_H(t) \quad (26)$$

where $\Delta\Theta_H(t)$ is HST rise over TOT and $t \in \mathbb{R}$ is time.

With the spatiotemporal oil temperature estimate $\hat{\Theta}_O(x, t)$, the winding temperature distribution, $\hat{\Theta}_W(x, t)$, is defined as follows:

$$\hat{\Theta}_W(x, t) = \hat{\Theta}_O(x, t) + \Delta\Theta_H(t) \quad (27)$$

where, $x, t \in \mathbb{R}$ are the position and time, respectively, $\hat{\Theta}_O(x, t)$ is the spatiotemporal oil temperature estimate. The hottest spatial temperature in Eq. (27) at each time instant t , corresponds to the HST in Eq. (26), i.e. $\max(\hat{\Theta}_W(\cdot, t)) = \Theta_H(t)$.

$\Delta\Theta_H(t)$ is the HST rise over TOT, which is given by:

$$\Delta\Theta_H(t) = \Delta\Theta_{H_1}(t) - \Delta\Theta_{H_2}(t) \quad (28)$$

where $\Delta\Theta_{H_1}(t)$ and $\Delta\Theta_{H_2}(t)$ model the oil heating considering the HST variations defined as follows [41]:

$$d\Delta\Theta_{H_i}(t) = v_i [\beta_i K(t)^y - \Delta\Theta_{H_i}(t)] \quad (29)$$

where $K(t)$ is the load factor [p.u.], y is the winding exponent constant, which models the loading exponential power with the heating of the windings, $i = \{1, 2\}$, $v_1 = \Delta t / k_{22} \tau_w$, $\beta_1 = k_{21} \Delta\Theta_{H,R}$ both for $i=1$, and $v_2 = k_{22} \Delta t / \tau_{TO}$, $\beta_2 = (k_{21}-1) \Delta\Theta_{H,R}$ both for $i=2$. $\Delta t = t - t'$, τ_w and τ_{TO} are the winding and oil time constants, k_{21} and k_{22} are the transformer thermal constants, and $\Delta\Theta_{H,R}$ is the HST rise at rated load. The operator d denotes a difference operation on Δt , such that $d\Delta\Theta_{H_i}(t) = \Delta\Theta_{H_i}(t) - \Delta\Theta_{H_i}(t')$ also for $i=\{1, 2\}$. To guarantee numerical stability, Δt should be small, never greater than half of the smaller time constant.

Under steady state, the initial condition, $\Theta_H(0)$, can be defined as:

$$\Theta_H(0) = \Theta_{TO}(0) + k_{21} \Delta\Theta_{H,R} K(0)^y - (k_{21}-1) \Delta\Theta_{H,R} K(0)^y \quad (30)$$

Eq. (30) allows iteratively estimating the next HST values, $\Theta_H(n\Delta t)$, $n \in \mathbb{Z}^+$, using Eqs. (26), (28), and (29).

A.3 Ageing Assessment

The IEC 60076-7 standard defines insulation ageing acceleration factor at time t , $V(t)$, as [41]:

$$V(t) = 2^{(\Theta_H(t)-98)/6} \quad (31)$$

Using the spatiotemporal winding temperature $\hat{\Theta}_W(x, t)$, the ageing acceleration factor at time t and position x , $V(x, t)$, can be defined as:

$$V(x, t) = 2^{(\hat{\Theta}_W(x, t)-98)/6} \quad (32)$$

The IEC 60076-7 assumes an expected life of 30 years, with a reference HST of 98°C [41]. The loss of life (LOL) at location x and time t can be defined as:

$$LOL(x, t) = \int_0^t V(x, t) dt \quad (33)$$

Consequently, the LOL at discrete time $L\Delta t$ and location x can be obtained by summing the ageing (cf. Eq. (32)) evaluated at the same time instants:

$$LOL(x, L\Delta t) = \sum_{n=0}^L V(x, n\Delta t) \quad (34)$$

where $n, L \in \mathbb{Z}^+$.

LOL can be converted into a recurrence relation for remaining useful life estimation [14].

A.4 Transformer Parameters

The transformer's nameplate parameters are summarized in Table 4.

Table 4: Transformer parameter values.

Parameter	Value
Rating [kVA], V_1/V_2	1100, 22000/400
R=Load losses/No load losses [W]	9800/842
$\Delta\Theta_{H,R}$ [°C]	15.1
k_{21}, k_{22}	2.32, 2.05
τ_0, τ_w [min.]	266.8, 9.75

B Benchmarking Models and Metrics

The proposed B-PINN approach is benchmarked against (i) a dropout based PINN implementation, which has been selected due to its computational efficiency [24] and (ii) the B-PINN homoscedastic counterpart which models epistemic and constant aleatoric sources of uncertainty [30].

B.1 Dropout-PINN

Dropout-PINN (d-PINN) extends the vanilla PINN (Section 2.1) by inserting dropout layers after each hidden layer, with a dropout rate, which is selected through a hyperparameter tuning process (introduced in Table 5). During training, dropout randomly deactivates a subset of neurons, acting as a regularization mechanism that improves generalization and mitigates overfitting [42]. Unlike standard inference, dropout is kept active at inference time. As illustrated in Fig. 12, M stochastic forward passes are performed during testing, each corresponding to a different realization of the dropout mask. This Monte Carlo sampling procedure yields an ensemble of network predictions whose empirical distribution enables the estimation of epistemic uncertainty through the computation of the predictive variance [24].

Finally, in order to capture the aleatoric uncertainty, and assuming that the uncertainty can be modelled with an equivalent Gaussian distribution, $N(\mu, \sigma)$, the d-PINN architecture has been modified adding an additional output which models variance, σ^2 . By modifying the architecture and employing a loss function based on NLL, the uncertainty can be learned as a function of data [36]:

$$\mathcal{L}_{NN}(y_{true}|\mu, \sigma^2) = \frac{1}{N} \sum_{i=1}^N \frac{(y_i - \mu(x_i))^2}{2\sigma(x_i)^2} + \frac{1}{2} \log \sigma(x_i)^2 \quad (35)$$

where y_i is the true value for the i -th element in the batch, $\mu(x_i)$ is the predicted mean value for the i -th element, and $\sigma(x_i)^2$ represents the variance.

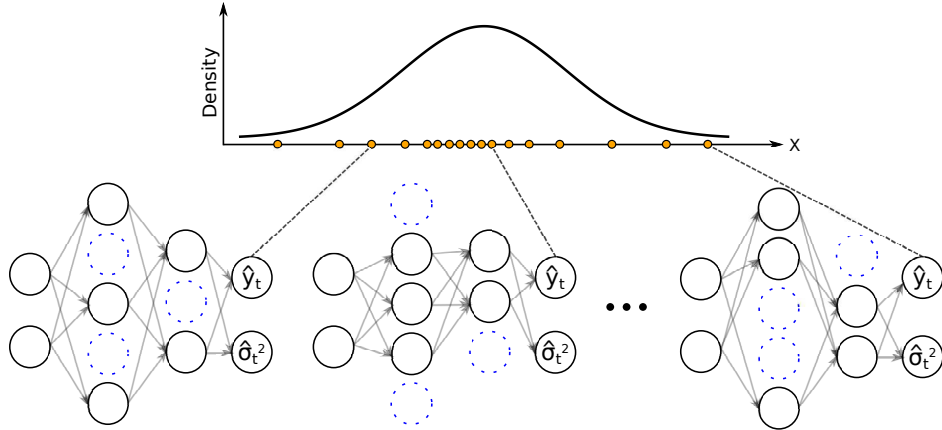


Figure 12: Use of dropout at inference stage with MC sampling.

The hyperparameters defined for the d-PINN model (Table 5) were tuned using the governing 1D heat diffusion partial differential equation (see Appendix A). The best results were obtained using the Adam optimizer with a learning rate of 0.01, a hyperbolic tangent activation function, and a fully connected architecture consisting of [2, 50, 50, 2] neurons.

Table 5: Architecture and optimization hyperparameters for d-PINN along with grid search range and final values.

Category	Hyperparameter	Grid	Value
Architecture	#Layers	2,3,4	2
	#Nodes	16,32,50,64	50
	Activation	ReLU,Tanh	Tanh
	Dropout rate	0.05,0.1,0.2,0.3	0.1
Optimization	Loss Function	-	-ELBO
	Optimizer	-	Adam
	Learning Rate	0.001,0.01,0.1	0.01
	Batch size	8,16,32	16
	#Epochs	5000,10000,15000	15000
	#MC inferences	50,100,200	200

The dropout rate strongly affects the quality of the estimated uncertainty. Consequently, a sensitivity analysis is conducted to identify the dropout rate that provides the most reliable uncertainty estimates, following the procedures in [15] and [30].

B.2 Bayesian PINN: Epistemic and Homoscedastic Uncertainty Quantification

This section presents the training algorithm of the Bayesian-PINN approach from [30], which integrates homoscedastic and epistemic uncertainty quantification. Figure 13 shows the overall approach and Algorithm 2 outlines the main steps to implement the Bayesian-PINN model using Variational Inference. Further details are provided in [30].

B.3 Metrics

The accuracy of probabilistic predictions is evaluated using three complementary metrics.

Negative Log Likelihood (NLL) evaluates how well a probabilistic model explains a given set of observations. It is defined as the negative logarithm of the likelihood function, which measures the probability of the observed data under a particular model [43]. For a model with parameters θ and observed data $X = \{x_1, \dots, x_n\}$, NLL is defined as:

$$\text{NLL}(\theta) = - \sum_{i=1}^n \log p(x_i | \theta) \quad (36)$$

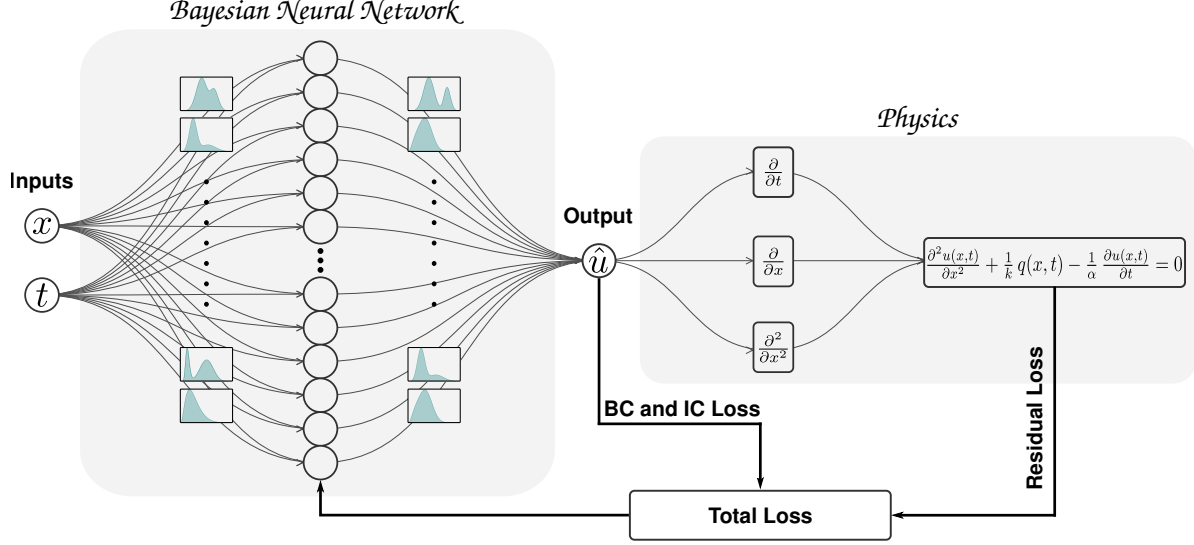


Figure 13: Bayesian-PINN approach with epistemic and homoscedastic uncertainty quantification for the probabilistic spatiotemporal transformer thermal model [30].

Algorithm 2 B-PINN Training via Variational Inference

- 1: **Input:** Collocation points (x_f, t_f) , initial condition data (x_0, u_0) , boundary condition data (x_{bc}, t_{bc}, u_{bc}) , prior distribution $p(\theta)$
- 2: Initialize variational parameters $w = \{\mu, \sigma\}$ for θ
- 3: **while** not converged **do**
- 4: Sample $\theta^{(i)} \sim q(\theta|w)$ via reparameterization trick
- 5: Evaluate predicted solution: $\hat{u}(x, t; \theta^{(i)})$
- 6: Compute residual: $r(x_f, t_f; \theta^{(i)}) = \mathcal{N}[\hat{u}](x_f, t_f; \theta^{(i)}) - f(x_f, t_f)$
- 7: Evaluate log-likelihood terms taking the log of Eq. (14)
- 8: Evaluate prior log-probability: $\log p(\theta^{(i)})$
- 9: Evaluate variational density: $\log q(\theta^{(i)}|w)$
- 10: Compute Monte Carlo estimate of ELBO loss via Eq. (15)
- 11: Update $w = \{\mu, \sigma\}$ using gradient $\nabla_w \mathcal{L}^{(i)}$
- 12: **end while**
- 13: **Return:** Learned variational posterior $q(\theta|w)$

where $p(x_i | \theta)$ is the probability of observation x_i given the model parameters. Minimizing the NLL is equivalent to maximizing the likelihood function, as the logarithm is a monotonically increasing function. NLL is particularly useful because it avoids numerical underflow with small probabilities and transforms the product of probabilities into a sum of log probabilities, which is more computationally stable [44].

Continuous Ranked Probability Score (CRPS) measures the discrepancy between the predicted Cumulative Distribution Function (CDF), $F(\cdot)$, and the observed empirical CDF for a given scalar observation y [45]:

$$CRPS(F, y) = \int (F(x) - \mathbb{1}(x \geq y))^2 dx, \quad (37)$$

where $\mathbb{1}(x \geq y)$ is the indicator function, which models the empirical CDF.

In order to obtain a single score value from Eq. (37), a weighted average is computed for each individual observation of the test set [46]:

$$CRPS = \frac{1}{N} \sum_{i=1}^N CRPS(F_i, y_i) \quad (38)$$

where N denotes the total number of predictions.